Available online at www.sciencedirect.com
SCIENCE DIRECT
Computers and Structures 84 (2006) 215–229
Computers & Structures
www.elsevier.com/locate/compstruc

A general three-dimensional L-section beam finite element for elastoplastic large deformation analysis

Phill-Seung Lee *, Ghyslaine McClure

Civil Engineering and Applied Mechanics, McGill University, Montreal, Quebec, Canada H3A 2K6

Received 22 April 2005; accepted 16 September 2005
Available online 15 November 2005

Abstract

In this paper, the development of a general three-dimensional L-section beam finite element for elastoplastic large deformation analysis is presented. We propose the generalized interpolation scheme for the isoparametric formulation of three-dimensional beam finite elements and the numerical procedure is developed for elastoplastic large deformation analysis. The formulation is general and effective for other thin-walled section beam finite elements. To show the validity of the formulation proposed, a 2-node three-dimensional L-section beam finite element is implemented in an analysis code. As numerical examples, we first perform elastic small and large deformation analyses of a cantilever beam structure subjected to various tip loadings, and elastoplastic large deformation analysis of the same structure under reversed cyclic tip loading. We then analyze the failures of simply supported beam structures of different lengths and slenderness ratios under elastoplastic large deformation. The same problems are solved using refined shell finite element models of the structures. The numerical results of the L-section beam finite element developed here are compared with the solutions obtained using shell finite element analyses. We also discuss the numerical solutions in detail.

Keywords: Beam structures; L-section beams; Finite elements; Nonlinear analysis; Elastoplastic material; Large deformation

1. Introduction

Thin-walled section beams including L-section (angle) shapes have been widely used in metallic frameworks for buildings, industrial structures and lattice structures. Nonlinear analysis considering large deformations and inelastic material is very important for investigating the load-bearing capacity of beam structures. In practice, the finite element method is the main tool for such analyses of beam structures [1]. The behavior of thin-walled beams (in particular, non-symmetric thin-walled sections) while undergoing inelastic large deformations is very complex and hard to predict using beam finite elements. In fact, the full three-dimensional nonlinear behavior of such sections can be represented more accurately using shell finite elements. However, for structures with a large number of thin-walled beam members, such as lattice structures, this approach is not practical because of the large modeling effort and computational time required.

Considerable effort has been put on the development of symmetric and non-symmetric section beam finite elements for elastic large deformation analysis and valuable results have been obtained, see Refs. [2–4] and therein. However, considering inelastic material, it is very hard to formulate such beam finite elements and only successes for relatively simple symmetric cross-sections (rectangular solid, I-shape, square and circular hollow sections [5–7]) have been reported. The development of general (symmetric or non-symmetric) section beam finite elements for inelastic large deformation analysis, which are simple and effective, is still open and the challenge is continuing.

In this paper, we propose a generalized interpolation scheme for the isoparametric formulation of three-dimensional beam finite elements, which can be used for both symmetric and non-symmetric section beams. The formulation

* Corresponding author. Tel.: +1 514 573 3477; fax: +1 514 398 7361.
E-mail address: phillseung@gmail.com (P.S. Lee).

0045-7949/$ - see front matter © 2005 Elsevier Ltd. All rights reserved.
doi:10.1016/j.compstruc.2005.09.013

and numerical procedure are developed for elastoplastic large deformation analysis of L-section beams. Note that the formulation is simple and effective for general (thin-walled) section beam finite elements. Since, in research articles, we could not find analysis examples or studies on three-dimensional L-section beam finite elements for elastoplastic large deformation analysis, we show the validity of the element proposed using the solution of shell finite element models.

The isoparametric approach has been widely used for the general curved beam finite element [1], because transverse shear strain is automatically considered and the formulation is general and effective, in particular, for nonlinear analysis. When the dimensions of the beam section are small compared to the beam length, the displacement-based isoparametric beam finite element locks, that is, the element is too stiff in bending problems. In spite of this disadvantage, this type of beam finite element is very attractive because the formulation is directly derived from three-dimensional continuum mechanics and easily extended to nonlinear analysis. Locking can be removed using reduced-order integration or a mixed formulation [1].

In this study, our main objective is to develop a general three-dimensional L-section beam finite element, which is general and reliable for elastoplastic large deformation analysis as well as linear elastic analysis. For effective nonlinear analysis of three-dimensional frameworks using beam finite elements, the following are necessary:

- Full three-dimensional behavior,
- Consideration of axial, bending and shearing actions,
- Availability for short and long beams (various slenderness ratios),
- Geometrical nonlinear capability (for large deformation and buckling behavior),
- Material nonlinear capability (in particular, for elastoplastic material),
- Consideration of loading and displacement eccentricities.

In the following sections, we present the isoparametric formulation of a general three-dimensional L-section beam finite element for elastoplastic large deformation analysis and show the numerical performance of the formulation. We propose the generalized geometry and displacement interpolation scheme for the isoparametric beam finite elements, which can automatically consider the eccentricities of loading and boundary conditions. To illustrate the application of this formulation and discuss its performance, we implement a 2-node L-section beam finite element in an analysis code. As numerical tests, we perform elastic small and large deformation analyses of an L-section cantilever beam structure subjected to various static loadings, and the elastoplastic large deformation analysis of the same structure under reversed cyclic tip loading. The failures of simply supported beam structures (of different length) under elastoplastic large deformation are analyzed. The results are compared with the solutions obtained with refined shell finite element models of the structures.

2. L-section beam finite element

In this section, we present the nonlinear formulation of the general three-dimensional L-section isoparametric beam finite element for elastoplastic large deformation analysis.

We first propose generalized geometry and displacement interpolations that can be used for beam finite elements of all possible section shapes, and we present the example of the L-section shape beam here. Considering large deformation and elastoplastic behavior, the updated Lagrangian formulation is adopted. We also use the "mixed interpolation of tensorial components" (MITC) technique for the locking removal [1,8]. To consider large rotation kinematics, the director vectors of the beam finite element are updated after each time increment using an orthogonal matrix for finite rotations as described in [9]. For elastoplastic analysis, we use the logarithmic strain calculated from the one-dimensional multiplicative decomposition of the longitudinal stretch of the beam [1].

In this paper, we use the superscript or subscript τ to denote time, but, in static analysis, τ is a dummy variable indicating load levels and incremental variables rather than actual time as in dynamic analysis [1].

2.1. Geometry and displacement interpolations

The basic kinematic assumption of the beam formulation is that plane cross-sections originally perpendicular to the central axis of the beam remain plane and undistorted under deformation but not necessarily perpendicular to the central axis of the deformed beam. In order to introduce a more general isoparametric beam formulation, instead of using the central axis, we use a longitudinal reference line, which does not need to pass through the centroid of the beam section. This reference line can be arbitrarily positioned on the beam section depending on the location of the nodal degrees of freedom; this feature automatically facilitates consideration of loading and displacement eccentricities at the finite element level.

Considering the longitudinal reference line in Fig. 1, the geometry of the q-node beam finite element at time τ is interpolated by

$$
{}^{\tau}\vec{x}(r,s,t) = \sum_{k=1}^{q} h_k(r)\,{}^{\tau}\vec{x}_k + \sum_{k=1}^{q} \frac{t-\bar{t}_k}{2} a_k h_k(r)\,{}^{\tau}\vec{V}_t^k + \sum_{k=1}^{q} \frac{s-\bar{s}_k}{2} b_k h_k(r)\,{}^{\tau}\vec{V}_s^k, \tag{1}
$$

where $h_k(r)$ are the interpolation polynomials in usual isoparametric procedures, ${}^{\tau}\vec{x}_k$ are the Cartesian coordinates of node k at time τ, a_k and b_k are the cross-sectional dimensions (length of legs in L-section shapes) at node k, and

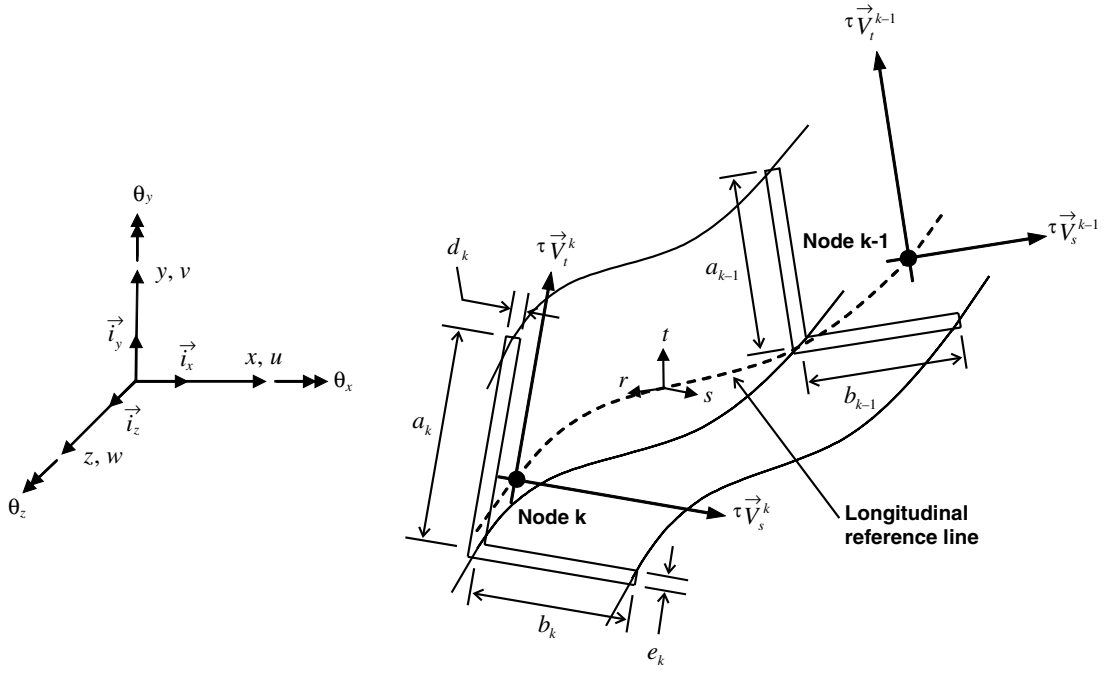

Fig. 1. Geometry of a general three-dimensional L-section beam element.

the unit vectors ${}^{\tau}\vec{V}_t^k$ and ${}^{\tau}\vec{V}_s^k$ are the director vectors in directions t and s at node k and at time τ. Note that ${}^{\tau}\vec{V}_t^k$ and ${}^{\tau}\vec{V}_s^k$ are normal to each other, and these vectors are parallel to the two legs of the L-section, as shown in Fig. 1.

In Eq. (1), the variables $\bar{s}_k$ and $\bar{t}_k$ are used to position the nodal degree of freedom (or the reference longitudinal line) in the beam finite element. In effect, these variables shift the domain in the natural coordinate system (s,t) as follows:

$$\begin{cases} -1 \leqslant s \leqslant 1 \\ -1 \leqslant t \leqslant 1 \end{cases} \Rightarrow \begin{cases} -1-\bar{s}_k \leqslant s-\bar{s}_k \leqslant 1-\bar{s}_k, \\ -1-\bar{t}_k \leqslant t-\bar{t}_k \leqslant 1-\bar{t}_k. \end{cases} \tag{2}$$

As illustrated in Fig. 2, $\bar{s}_k$ and $\bar{t}_k$ are calculated from the location of the nodal degree of freedom and the cross-sectional dimensions. Let us consider the nodal Cartesian coordinate system defined by the director vectors ${}^{\tau}\vec{V}_t^k$ and ${}^{\tau}\vec{V}_s^k$ at node k. The points c and c' are the position of the nodal degree of freedom and the center of the dotted rectangle, respectively. Due to the geometrical proportionality between Fig. 2(a) and (b), we obtain

$$\bar{s}_k = 2\frac{\bar{x}_k}{b_k}, \quad \bar{t}_k = 2\frac{\bar{y}_k}{a_k}, \tag{3}$$

where $\bar{x}_k$ and $\bar{y}_k$ represent the projected distances between c and c' in the nodal Cartesian coordinate system at node k. This shifting of the domain in the natural coordinate system allows a general description of the geometry interpolation. Consequently, the positions of the nodal degrees of freedom can be arbitrarily located on the beam sections.

The Cartesian coordinate of a point at time $\tau+\Delta\tau$ is

$${}^{\tau+\Delta\tau}\vec{x} = {}^{\tau}\vec{x} + {}^{\tau}\vec{u}, \tag{4}$$

where ${}^{\tau}\vec{u}$ is the incremental displacement from time τ to $\tau+\Delta\tau$.

Substituting Eq. (1) into Eq. (4) and using the second-order approximations for the large rotation of the director vectors, we obtain the incremental displacement from time τ to $\tau+\Delta\tau$

$${}^{\tau}\vec{u} = {}^{\tau}\vec{u}^a + {}^{\tau}\vec{u}^b \tag{5}$$

with

$$\begin{aligned} {}^{\tau}\vec{u}^a(r,s,t) &= \sum_{k=1}^{q} h_k(r)\,{}^{\tau}\vec{u}_k + \sum_{k=1}^{q} \frac{t-\bar{t}_k}{2} a_k h_k(r)\left[{}^{\tau}\vec{\theta}_k \times {}^{\tau}\vec{V}_t^k\right] \\ &\quad + \sum_{k=1}^{q} \frac{s-\bar{s}_k}{2} b_k h_k(r)[{}^{\tau}\vec{\theta}_k \times {}^{\tau}\vec{V}_s^k], \\ {}^{\tau}\vec{u}^b(r,s,t) &= \sum_{k=1}^{q} \frac{t-\bar{t}_k}{4} a_k h_k(r)\left[{}^{\tau}\vec{\theta}_k \times ({}^{\tau}\vec{\theta}_k \times {}^{\tau}\vec{V}_t^k)\right] \\ &\quad + \sum_{k=1}^{q} \frac{s-\bar{s}_k}{4} b_k h_k(r)[{}^{\tau}\vec{\theta}_k \times ({}^{\tau}\vec{\theta}_k \times {}^{\tau}\vec{V}_s^k)], \end{aligned} \tag{6}$$

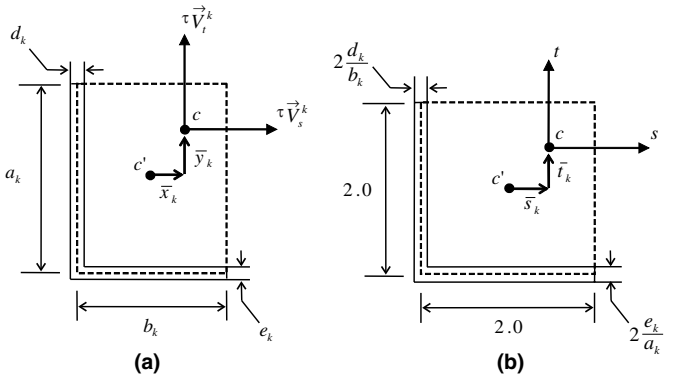

Fig. 2. Geometric description of $\bar{x}_k$, $\bar{y}_k$, $\bar{s}_k$ and $\bar{t}_k$ at node k: (a) in the nodal Cartesian coordinate system and (b) in the natural coordinate system.

in which the incremental rotation vector at node k is

$$ {}^{\tau}\vec{\theta}_k = \begin{bmatrix} {}^{\tau}\theta_x^k \\ {}^{\tau}\theta_y^k \\ {}^{\tau}\theta_z^k \end{bmatrix}, \tag{7} $$

and the displacement ${}^{\tau}\vec{u}^b$ is the additional term derived from the second-order approximations for the large rotation of the director vectors. Of course, this term is not necessary for linear analysis. This additional displacement is a quadratic expression in rotations and is used for the nonlinear formulation of the beam finite element.

2.2. Finite element discretization

Using the principle of virtual displacement at time $\tau+\Delta\tau$, the linearized equilibrium equation in the updated Lagrangian formulation is obtained for the beam finite element,

$$ \int_{{}_{\tau}V} {}_{\tau}C_{ijkm}\, {}_{\tau}e^a_{km}\delta_{\tau}e^a_{ij}\,\mathrm{d}^{\tau}V + \int_{{}_{\tau}V} {}^{\tau}\tau_{ij}(\delta_{\tau}\eta^a_{ij}+\delta_{\tau}e^b_{ij})\,\mathrm{d}^{\tau}V = {}^{\tau+\Delta\tau}\Re - \int_{{}_{\tau}V} {}^{\tau}\sigma_{ij}\delta_{\tau}e^a_{ij}\,\mathrm{d}^{\tau}V, \tag{8} $$

where ${}^{\tau}V$, ${}_{\tau}C_{ijkm}$ and ${}^{\tau}\sigma_{ij}$ are the volume, the material law and the Cauchy stress tensor at time τ, respectively, and ${}_{\tau}e^a_{km}=\frac{1}{2}({}^{\tau}u^a_{k,m}+{}^{\tau}u^a_{m,k})$ are the linear terms of the strain tensor corresponding to the displacement ${}^{\tau}\vec{u}^a$ at time τ, $\delta_{\tau}e^a_{ij}=\frac{1}{2}(\delta^{\tau}u^a_{i,j}+\delta^{\tau}u^a_{j,i})$ are the linear terms of the strain tensor corresponding to the virtual displacement $\delta^{\tau}\vec{u}^a$ at time τ, $\delta_{\tau}\eta^a_{ij}=\frac{1}{2}(\delta^{\tau}u^a_{k,i}\,{}^{\tau}u^a_{k,j}+{}^{\tau}u^a_{k,i}\delta^{\tau}u^a_{k,j})$ are the nonlinear terms of the strain tensor corresponding to the virtual displacement $\delta^{\tau}\vec{u}^a$ at time τ, and $\delta_{\tau}e^b_{ij}=\frac{1}{2}(\delta^{\tau}u^b_{i,j}+\delta^{\tau}u^b_{j,i})$ are the components of the strain tensor corresponding to the virtual displacement $\delta^{\tau}\vec{u}^b$ at time τ.

The term ${}^{\tau+\Delta\tau}\Re$ in the right-hand side of Eq. (8) represents the externally applied forces,

$$ {}^{\tau+\Delta\tau}\Re = \int_{{}_{\tau+\Delta\tau}V} {}^{\tau+\Delta\tau}f_i^B\delta u_i\,\mathrm{d}^{\tau+\Delta\tau}V + \int_{{}_{\tau+\Delta\tau}S_f} {}^{\tau+\Delta\tau}f_i^S\delta u_i^S\,\mathrm{d}^{\tau+\Delta\tau}S, \tag{9} $$

where ${}^{\tau+\Delta\tau}f_i^B$ are the components of the externally applied force per unit volume at time $\tau+\Delta\tau$, ${}^{\tau+\Delta\tau}f_i^S$ are the components of the externally applied surface traction per unit surface area at time $\tau+\Delta\tau$, ${}^{\tau+\Delta\tau}S_f$ is the surface at time $\tau+\Delta\tau$ on which external tractions are applied, and δu_i^S are δu_i evaluated on the surface ${}^{\tau+\Delta\tau}S_f$.

Substituting Eqs. (1) and (6) into (8), we obtain the matrix form of the linearized equilibrium equation in the updated Lagrangian formulation [1],

$$ {}^{\tau}\mathbf{K}\,{}^{\tau}\mathbf{U} = {}^{\tau+\Delta\tau}\mathbf{R} - {}^{\tau}\mathbf{F}, \tag{10} $$

where ${}^{\tau}\mathbf{K}$ is the tangent stiffness matrix at time τ, ${}^{\tau}\mathbf{U}$ is the incremental nodal displacement vector, ${}^{\tau+\Delta\tau}\mathbf{R}$ is the vector of externally applied nodal load at time $\tau+\Delta\tau$, and ${}^{\tau}F$ is the vector of nodal forces equivalent to the element stresses at time τ. ${}^{\tau}\mathbf{K}$ consists of both the geometric linear and nonlinear stiffness matrices (${}^{\tau}\mathbf{K}={}^{\tau}\mathbf{K}_{\mathrm{L}}+{}^{\tau}\mathbf{K}_{\mathrm{NL}}$).

2.3. Numerical integration

In order to obtain the tangent stiffness matrix and vectors of Eq. (10), we perform the numerical integration over the two legs of the L-section, which are placed in the $r-t$ and $r-s$ planes (see Figs. 1–3),

$$ \int_V \mathbf{A}\,\mathrm{d}V = \int_{-1}^{1}\int_{-1}^{1}[\eta_{rt}\mathbf{A}\det\mathbf{J}]_{s=-1}\,\mathrm{d}t\,\mathrm{d}r + \int_{-1}^{1}\int_{-1}^{1}[\eta_{\mathrm{rs}}\mathbf{A}\det\mathbf{J}]_{t=-1}\,\mathrm{d}s\,\mathrm{d}r, \tag{11} $$

where $\mathbf{A}$ is a generic matrix or vector function, det$\mathbf{J}$ is the determinant of the three-dimensional Jacobian matrix and the factors η_{rt} and η_{rs} are

$$ \eta_{\mathrm{rt}} = 2\sum_{k=1}^{q}h_k(r)d_k \Big/ \sum_{k=1}^{q}h_k(r)b_k, \qquad \eta_{\mathrm{rs}} = 2\sum_{k=1}^{q}h_k(r)e_k \Big/ \sum_{k=1}^{q}h_k(r)a_k \tag{12} $$

Gaussian quadrature is used for the integration in Eq. (11). For example, Fig. 3 shows the eight integration points for the elastic analysis of the 2-node L-section beam finite element and the coordinates of the integration points are given in Table 1. Of course, more integration points in the s and t directions are required for inelastic analysis and the solution accuracy depends on the number of integration points. This is further discussed in Section 3.

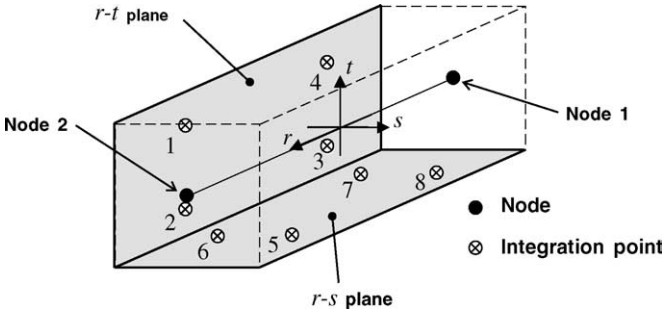

Fig. 3. Gauss integration points of the 2-node L-section beam element in the natural coordinate system.

Table 1
Integration points in the natural coordinate system for elastic analysis

r–t plane				r–s plane			
i	r	s	t	i	r	s	t
1	$1/\sqrt{3}$	-1	$1/\sqrt{3}$	5	$1/\sqrt{3}$	$1/\sqrt{3}$	-1
2	$1/\sqrt{3}$	-1	$-1/\sqrt{3}$	6	$1/\sqrt{3}$	$-1/\sqrt{3}$	-1
3	$-1/\sqrt{3}$	-1	$-1/\sqrt{3}$	7	$-1/\sqrt{3}$	$-1/\sqrt{3}$	-1
4	$-1/\sqrt{3}$	-1	$1/\sqrt{3}$	8	$-1/\sqrt{3}$	$1/\sqrt{3}$	-1

2.4. MITC technique

The standard displacement-based isoparametric beam finite element is too stiff in bending-dominated problems when the element is thin, regardless of the displacement interpolation order. In other words, the solution convergence of the beam finite element discretization in bending-dominated problems deteriorates significantly as the ratio of the dimensions of the beam section (a_k and b_k) to the beam length decreases. This major difficulty encountered in the finite element analysis of beams is called "locking". Effective finite element discretizations for beam analysis should not lock.

We use the well-known "mixed interpolation of tensorial components" (MITC) technique for locking removal of the L-section beam finite element. The basic idea of the MITC technique is to interpolate displacements and strains separately and connect these interpolations at tying points [1,8].

For beam finite elements, the transverse shear and normal covariant strain components are interpolated,

$$\hat{\varepsilon}_{ij}(r,s,t) = \sum_{k=1}^{n_{ij}} h^k(r)\tilde{\varepsilon}_{ij}(r^k,s,t), \tag{13}$$

where $\hat{\varepsilon}_{ij}(r,s,t)$ are assumed covariant strain components in the beam finite element, $\tilde{\varepsilon}_{ij}(r^k,s,t)$ are the covariant strain components calculated from the displacement-based beam finite element at tying point (r^k,s,t)

$$\tilde{\varepsilon}_{ij} = \frac{1}{2}\left(\frac{\partial\vec{u}}{\partial r_i}\cdot\frac{\partial\vec{x}}{\partial r_j} + \frac{\partial\vec{x}}{\partial r_j}\cdot\frac{\partial\vec{u}}{\partial r_i} + \frac{\partial\vec{u}}{\partial r_i}\cdot\frac{\partial\vec{u}}{\partial r_j}\right)$$
$$\text{with } r_1 = r,\ r_2 = s,\ r_3 = t, \tag{14}$$

and $h^k(r)$ are the assumed interpolation functions satisfying

$$h^k(r^l) = \delta_{kl} \quad (\delta_{ij} = 1 \text{ if } i = j \text{ and } 0 \text{ otherwise}),$$
$$k,l = 1,\ldots,n_{ij}. \tag{15}$$

The assumed strain components and the tying points depend on the displacement interpolation functions used (or the number of element nodes). As an example, for the 2-node isoparametric beam finite element, we use one tying point at $r = 0$ for the covariant strains $\tilde{\varepsilon}_{rs}$ and $\tilde{\varepsilon}_{tr}$ but two tying points at $r = \pm\frac{1}{\sqrt{3}}$ for the covariant strains $\tilde{\varepsilon}_{rs}$, $\tilde{\varepsilon}_{tr}$ and $\tilde{\varepsilon}_{rr}$ need to be used for the 3-node element in general.

2.5. Large rotation

After solving Eq. (10) in each incremental step, we obtain the incremental nodal displacement and rotation. We then update the nodal coordinate and director vectors at node k for time $\tau+\Delta\tau$ using Eq. (4) and

$${}^{\tau+\Delta\tau}\vec{V}_t^k = {}^{\tau}\mathbf{Q}\,{}^{\tau}\vec{V}_t^k, \quad {}^{\tau+\Delta\tau}\vec{V}_s^k = {}^{\tau}\mathbf{Q}\,{}^{\tau}\vec{V}_s^k, \tag{16}$$

where ${}^{\tau}\mathbf{Q}$ is an orthogonal matrix for finite rotation [9],

$${}^{\tau}\mathbf{Q} = \mathbf{I} + \frac{\sin{}^{\tau}\gamma_k}{{}^{\tau}\gamma_k}{}^{\tau}\mathbf{S}_k + \frac{1}{2}\left(\frac{\sin\frac{{}^{\tau}\gamma_k}{2}}{\frac{{}^{\tau}\gamma_k}{2}}\right)^2{}^{\tau}\mathbf{S}_k^2 \tag{17}$$

with

$${}^{\tau}\gamma_k = \{({}^{\tau}\theta_x^k)^2 + ({}^{\tau}\theta_y^k)^2 + ({}^{\tau}\theta_z^k)^2\}^{\frac{1}{2}},$$
$${}^{\tau}\mathbf{S}_k = \begin{bmatrix} 0 & -{}^{\tau}\theta_z^k & {}^{\tau}\theta_y^k \\ {}^{\tau}\theta_z^k & 0 & -{}^{\tau}\theta_x^k \\ -{}^{\tau}\theta_y^k & {}^{\tau}\theta_x^k & 0 \end{bmatrix}. \tag{18}$$

2.6. Elastoplastic material model

In three-dimensional large strain elastoplasticity, the multiplicative decomposition of the deformation gradient from time 0 to τ is generally used,

$${}^{\tau}_{0}\mathbf{X} = {}^{\tau}_{0}\mathbf{X}^E\,{}^{\tau}_{0}\mathbf{X}^P, \tag{19}$$

where ${}^{\tau}_{0}\mathbf{X}^E$ and ${}^{\tau}_{0}\mathbf{X}^P$ are, respectively, the elastic and plastic deformation gradients [1]. For the beam finite element formulation, we use the one-dimensional multiplicative decomposition,

$${}^{\tau}_{0}\lambda = {}^{\tau}_{0}\lambda^E\,{}^{\tau}_{0}\lambda^P, \tag{20}$$

where ${}^{\tau}_{0}\lambda$ is the stretch in the longitudinal direction of the beam finite element and, ${}^{\tau}_{0}\lambda^E$ and ${}^{\tau}_{0}\lambda^P$ are, respectively, the elastic and plastic stretches. In Eq. (20), the stretch is given by

$${}^{\tau}_{0}\mathbf{X} = \left({}^{0}\vec{n}^T\,{}^{\tau}_{0}\mathbf{X}^T\,{}^{\tau}_{0}\mathbf{X}\,{}^{0}\vec{n}\right)^{1/2}, \tag{21}$$

where ${}^{0}\vec{n}$ is the unit vector of the longitudinal direction of the beam finite element,

$${}^{0}\vec{n} = \frac{{}^{0}\vec{r}}{|{}^{0}\vec{r}|} \quad \text{with } {}^{0}\vec{r} = \frac{\partial{}^{0}\vec{x}}{\partial r}. \tag{22}$$

Of course, the three-dimensional multiplicative decomposition in Eq. (19) can be used to obtain more accurate solutions. However, the one-dimensional multiplicative decomposition requires less computational time, in particular when the shearing effects are relatively smaller than the bending effects, as is usually the case.

The logarithmic normal strain,

$${}^{\tau}\varepsilon_{nn} = \ln{}^{\tau}_{0}\lambda, \tag{23}$$

and the normal component of the Cauchy stress, ${}^{\tau}\sigma_{nn}$, in the longitudinal direction are used and the bilinear elastoplastic stress–strain relation with isotropic strain hardening shown in Fig. 4 is used.

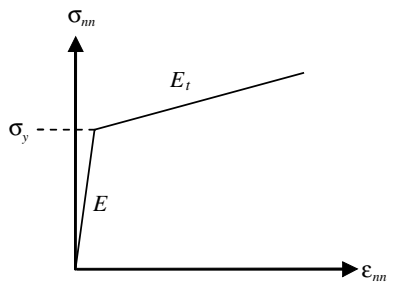

Fig. 4. Stress–strain relationship of bilinear elastoplastic material.

3. Numerical tests

To investigate in detail the predictive capability of the proposed numerical scheme, we implement the 2-node L-section beam finite element in an analysis code and perform numerical studies for various beam problems. In this section, we report upon the various numerical results of the L-section beam finite element proposed in this study.

Let us consider the beam structure shown in Fig. 5. The beam is straight and has an L-shape section with two legs of lengths, W and H. The legs have a constant thickness, h, and are normal to each other. The section profile is constant along the beam axis. The beam is then given various boundary conditions and loadings at ends A and B, which allows to simulate various structural behaviors. In the following section, we perform the elastic small and large deformation, elastoplastic large deformation and elastoplastic failure analyses using the 2-node beam finite elements developed.

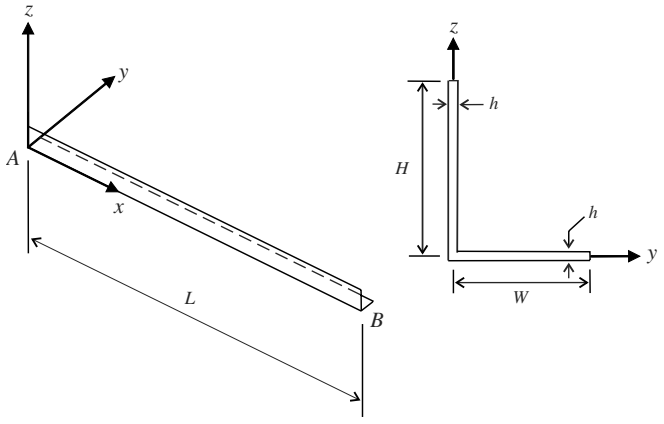

Fig. 5. L-section beam structure.

The results obtained with the beam finite elements are compared with the refined solutions of the MITC9 shell finite elements in ADINA [10]. The reliable performance of the MITC9 shell finite element has been demonstrated in the literature [11,12]. For the shell finite element models, a uniform mesh is used in each leg and along the axial direction and for the beam finite element models, a uniform mesh of 2-node beam elements is used along the axial direction. Fig. 6 shows the meshes used for the shell (2×20 elements) and beam (eight elements) finite element models. After studying the solution convergence of the shell finite element models, we selected the mesh of the shell finite element models which can be used as reference.

In this study, we use only uniform meshes, which is not optimal for efficient numerical solution in general. However, since uniform meshes are frequently used in practice, it is valuable to use them to investigate the numerical performance of the proposed beam finite element.

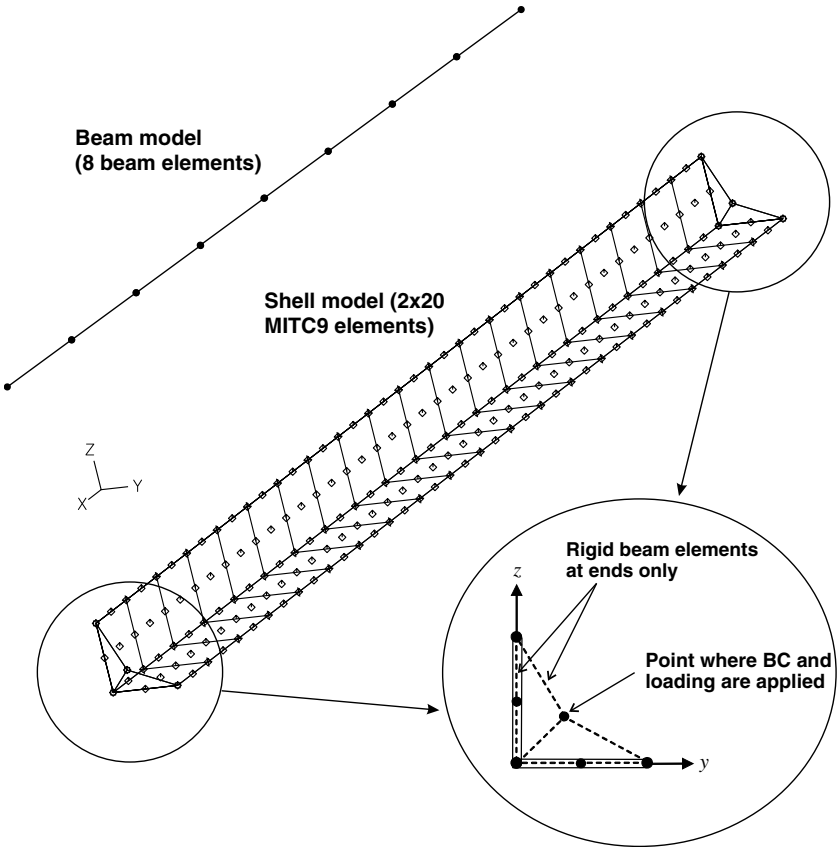

Fig. 6. Beam and shell finite element models of the L-section beam structure.

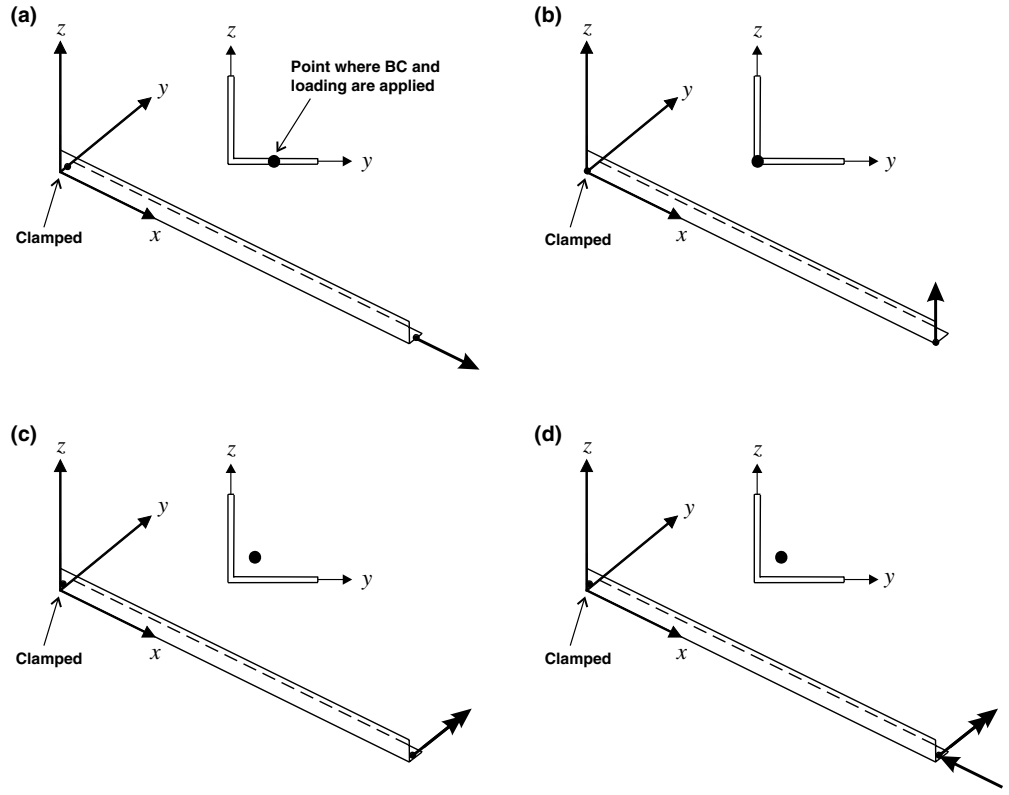

Fig. 7. Load cases for the elastic analyses of the cantilever L-section beam structure. (a) $F_x = 1.0$ N, (b) $F_z = 1.0$ N, (c) $M_y = 1.0$ N m, (d) $F_x = -\alpha N$ and $M_y = \alpha$ N m.

In order to avoid local failures near the ends of the beam structure in the shell finite element models due to concentrated loading and boundary conditions, we impose the kinematic beam assumptions at the ends as mentioned in Section 2.1. For that purpose, we use rigid beam finite elements[1] at the two ends of the beam structure as shown with the dotted lines in Fig. 6.

3.1. Cantilever L-section beam problems

We first analyze a cantilever L-section beam structure with the sectional dimensions $W = H = 0.0508$ m and $h = 0.0032$ m. The beam structure of m in Fig. 5 is clamped at point A and free at point B. The structure is loaded with forces and moments at point$B$. In the sections of the beam ends, the boundary conditions and loads are applied at:

- Case (a): the center of the leg in the y-direction ($y = 0.0254$ m and $z = 0.0$ m)
- Case (b): the shear center ($y = z = 0.0$ m)
- Cases (c) and (d): the bending center (centroid) of the beam section ($y = z = W/4 = 0.0127$ m in Fig. 5; $W/4$ is a good approximation when $h \ll W$).

Considering the various cases of static loading as shown in Fig. 7(a)–(d), we perform the elastic small and large deformation analyses and the elastoplastic large deformation analysis under reversed cyclic loading.

3.1.1. Elastic small and large deformation analyses

Considering three load cases at the tip shown in Fig. 7(a)–(c), we perform the elastic small deformation analyses of the cantilever L-section beam problem. An elastic material is used (Young's modulus; $E = 2 \times 10^{11}$ N/m^2 and Poisson's ratio; $\nu = 0.3$) for steel.

As mentioned before, we use the uniformly distributed 2, 4 and 8 L-section beam finite element meshes for the beam models and a uniform 4×80 mesh of the MITC9 shell finite elements for the reference shell model. Table 2 reports that the results calculated from the two models are very close when the MITC technique is used for the L-section beam finite element but the L-section beam finite element without using the MITC technique clearly locks. In cases (a) and (c), the solutions of the beam finite element using the MITC technique are accurate enough regardless of the mesh refinements.

We then investigate the performance of the proposed L-section beam finite element in the elastic large deformation

[1] Note that using such rigid beam finite elements cannot perfectly satisfy the kinematic beam assumption at the beam ends because the elements restrain the in-plane deformation along the legs of the beam section, that is, this modeling restricts the expansions of the shell finite elements due to Poisson's effect locally at the beam ends. However, this effect is local and negligible in the global response of the beam.

Table 2
Tip displacements calculated in the linear elastic analyses of the cantilever L-section beam structure using the MITC technique

Mesh	Case (a)		Case (b)		Case (c)	
	δ_x	$-\delta_y$, δ_z	δ_y	δ_z	δ_y	δ_z
Beam (1el.)	1.07653e−7	3.63282e−6	8.58098e−4	1.43045e−3	−4.29073e−4	−7.15122e−4
Beam (2el.)	1.07653e−7	3.63282e−6	1.07264e−3	1.78801e−3	−4.29073e−4	−7.15122e−4
Beam (4el.)	1.07653e−7	3.63282e−6	1.12627e−3	1.87740e−3	−4.29073e−4	−7.15122e−4
Beam (8el.)	1.07653e−7	3.63282e−6	1.13968e−3	1.89975e−3	−4.29073e−4	−7.15122e−4
Beam (8el.)[a]	1.00407e−9	3.06232e−9	5.45709e−8	1.21179e−7	−2.07250e−8	−4.48377e−8
Shell (4 × 80el.)	1.07570e−7	3.62781e−6	1.13804e−3	1.90033e−3	−4.26848e−4	−7.12577e−4

[a] Denotes the beam finite element without using the MITC technique and unit for displacement is m.

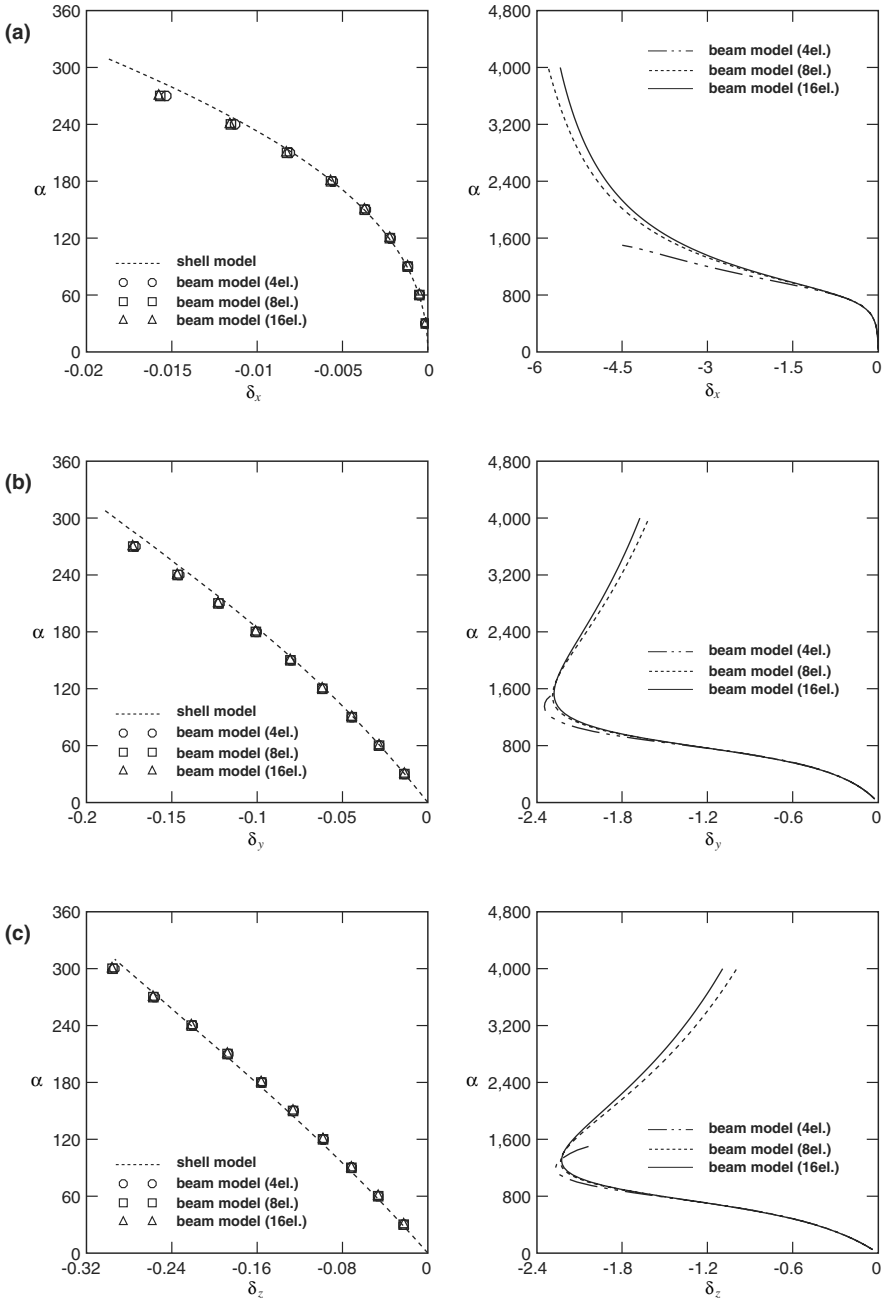

Fig. 8. Load–displacement curves for the x, y and z-directional tip displacements (unit for displacement is m).

analysis. The cantilever L-section beam is subjected to the tip loading shown in Fig. 7(d) and the elastic large deformation analysis is performed using the same elastic material (steel) as in the elastic small deformation analyses. The loading factor α is increased statically and the tip displacements in the x, y and z directions are measured. We calculate the solutions using the uniform 4×80 mesh of the shell model and the uniform 4, 8 and 16 element meshes of the beam model.

Fig. 8 shows the load–displacement (α–δ) curves in the two ranges of loading (up to $\alpha = 300$ and $\alpha = 4000$). The solutions of the shell finite element model are not obtained for the loading factor larger than $\alpha = 300$ due to local failure in the numerical solution. When 4, 8 and 16 L-section beam finite elements are used in the beam model up to $\alpha = 300$, the responses of the L-section beam finite elements agree with those of the shell finite element model. The load–displacement curves up to $\alpha = 4000$ show that the solution of the beam model using 4 L-section beam finite elements lacks accuracy compared to the solutions obtained with 8 and 16 L-section beam finite elements in

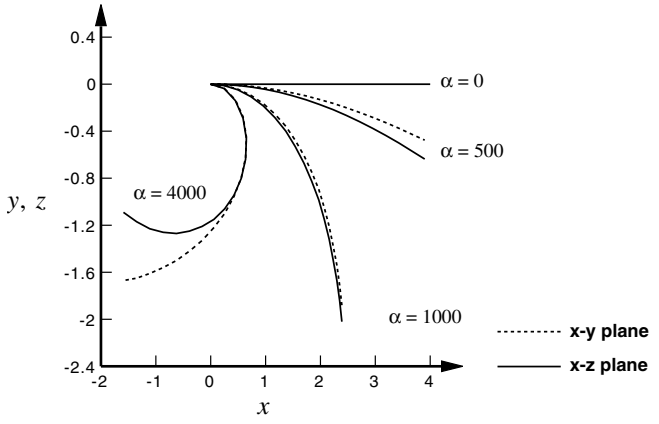

Fig. 9. Deformed shapes projected in the x–y and x–z planes for a mesh of 16 elements (unit is m).

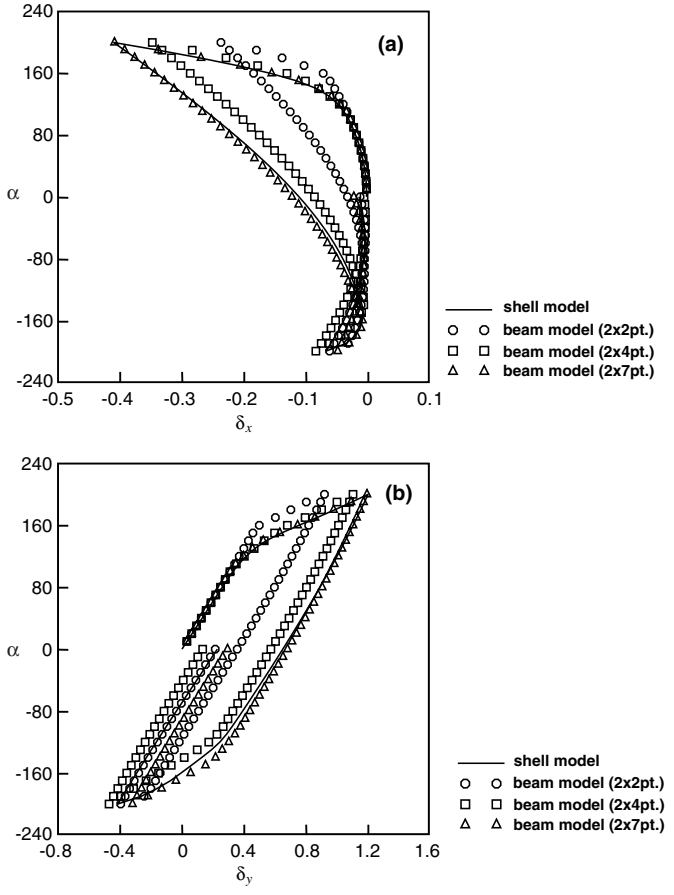

Fig. 11. Load–displacement curves for the (a) x- and (b) y-directional tip displacements (unit for displacement is m).

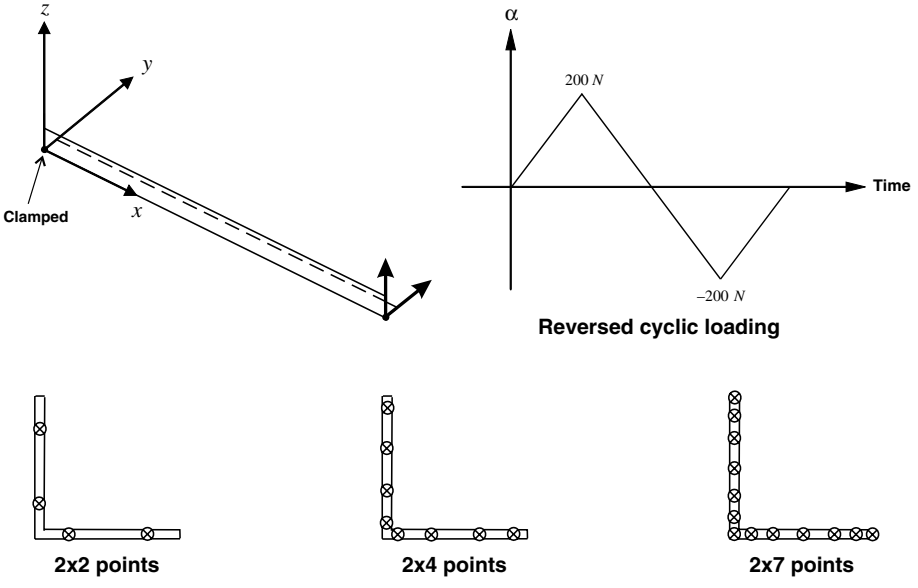

Fig. 10. Static reversed cyclic loading ($F_y = F_z = \alpha N$) and numerical integration points used in the beam section.

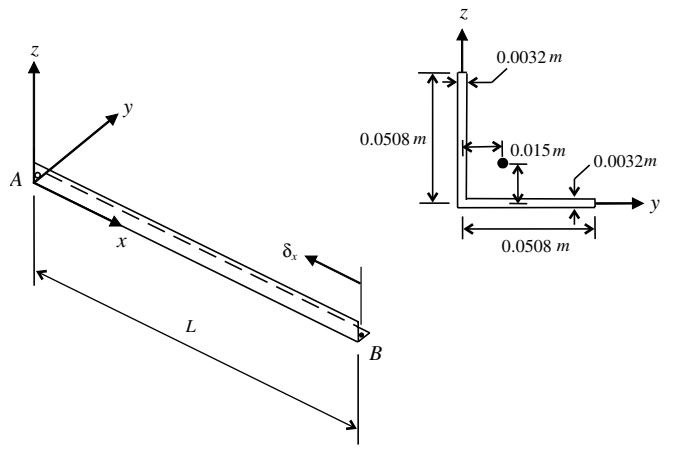

Fig. 12. A simply supported L-section beam with a section of equal legs.

the very large deformation range. Fig. 9 displays the deformed shapes of the cantilever projected in the x–y and x–z planes at various load levels for the case with a mesh of 16 beam finite elements.

3.1.2. Elastoplastic large deformation analysis

We perform here the elastoplastic large deformation analysis under a reversed cyclic loading using the beam and shell finite element models described in the previous section. The properties of the bilinear elastoplastic material (see Fig. 4) used are:

- Young's modulus: $E = 2 \times 10^{11}$ N/m^2,
- Yield stress: $\sigma_y = 250 \times 10^6$ N/m^2,
- Poisson's ratio: $v = 0.3$,
- Strain hardening modulus: $E_t = 2.0 \times 10^{10}$ N/m^2.

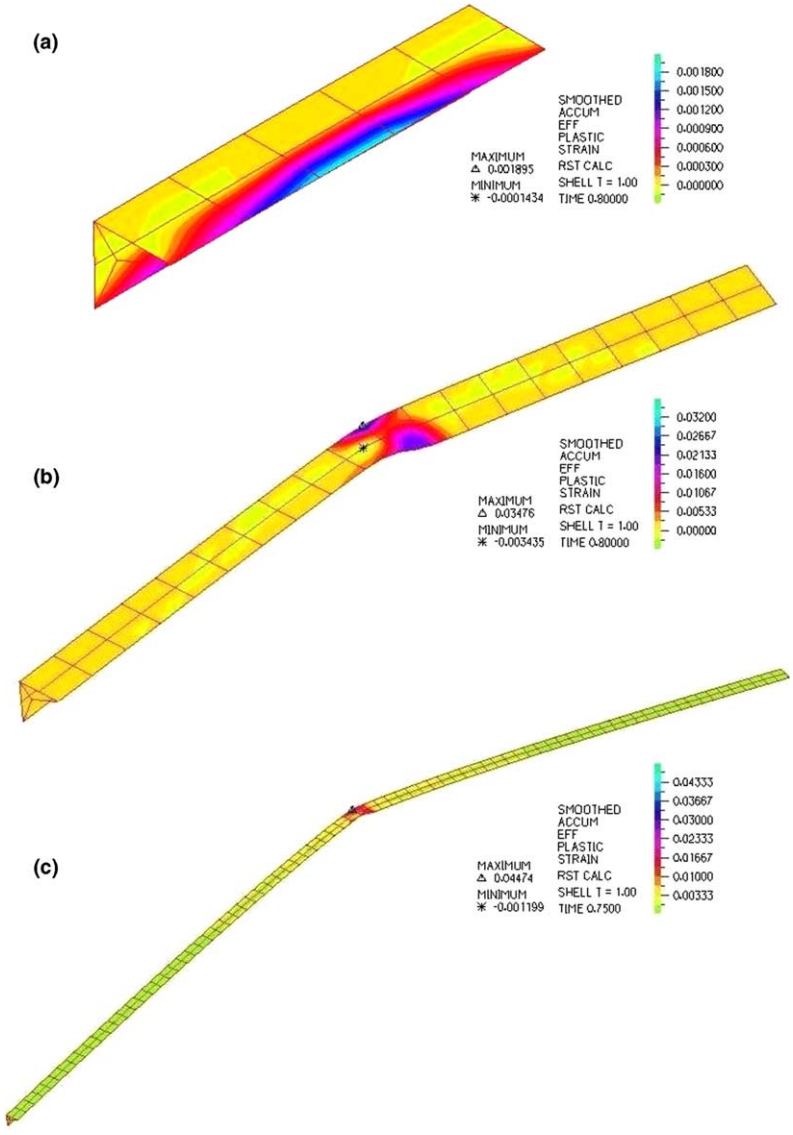

Fig. 13. Non-scaled deformed shapes and accumulated effective plastic strain distributions. (a) $L = 0.25$ m, $\delta_x = 0.0004$ m (2×5el. mesh), (b) $L = 1.0$ m, $\delta_x = 0.008$ m (4×20 el. mesh), (c) $L = 4.0$ m, $\delta_x = 0.06$ m (4×80 el. mesh).

As shown in Fig. 10, a reversed cyclic loading is statically applied at the shear center of the free end of the beam ($y = z = 0.0$ m in Fig. 5). We use the uniform 4×80 mesh for the reference shell model and the uniform 8 element mesh of L-section beam finite elements for the beam finite element model. Varying the number of numerical integration points as shown in Fig. 10, the solutions are calculated.

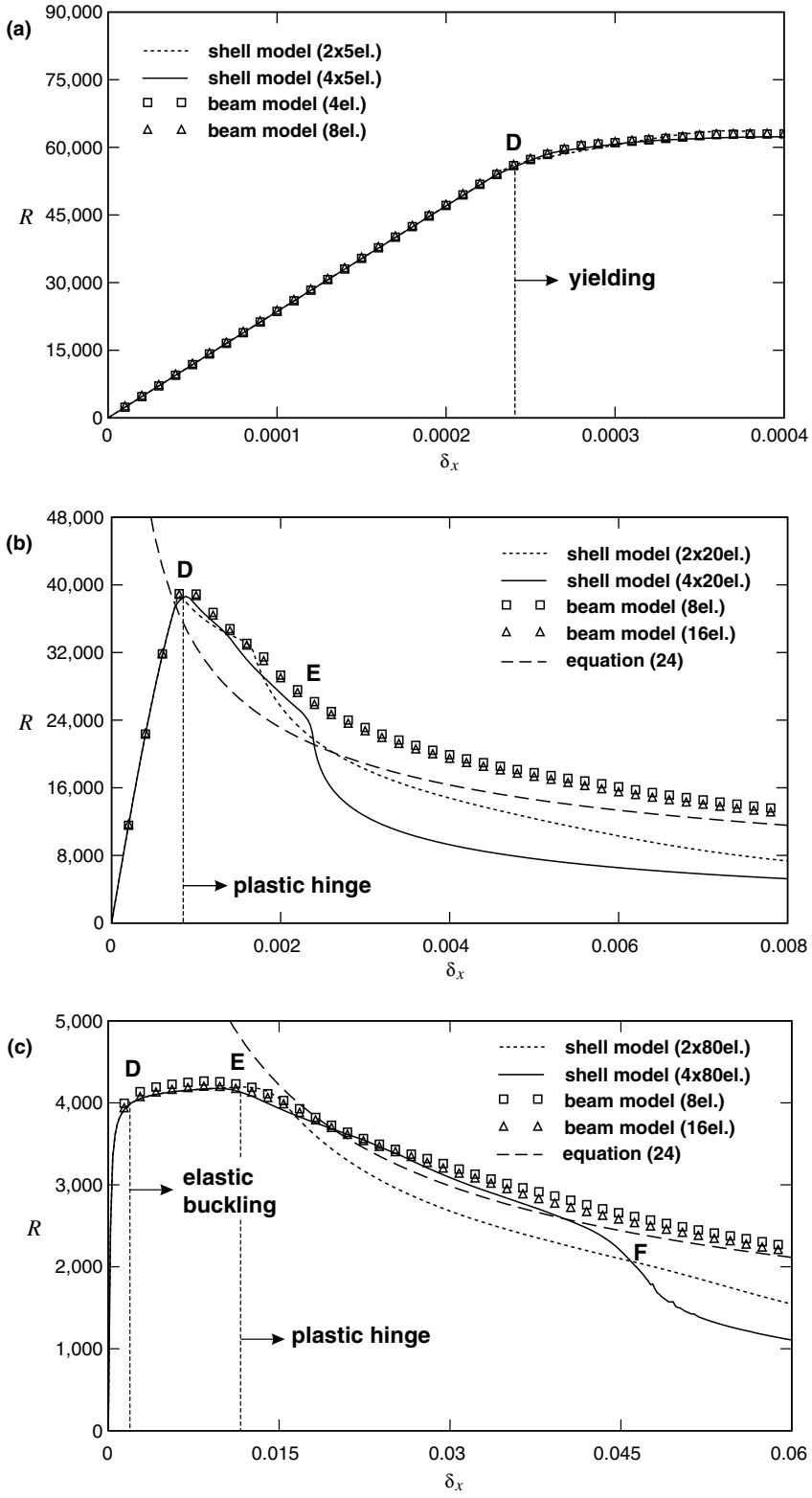

Fig. 14. Reaction–displacement curves for (a) $L = 0.25$ m and (b) $L = 1.0$ m and (c) $L = 4.0$ m. (Unit for reaction is N and unit for displacement is m.)

Fig. 11(a) and (b) display the load–displacement curves for the x- and y-directional tip displacements, respectively. Due to the symmetry of the problem, the z-directional displacement is equal to the y-directional displacement. After one cycle of loading, the residual displacements due to plastic strain are observed. As the number of integration points increases, the solutions of the beam finite element model converge toward the reference shell finite element solutions. When the 7-point numerical integration scheme is used in each leg of the beam section, the responses calculated using the L-section beam finite elements show very good agreement with the reference solutions obtained with the MITC9 shell finite element model. The 7-point numerical integration is therefore recommended for inelastic analysis using the L-section beam finite element proposed in this paper.

3.2. Elastoplastic failure analyses of a simply supported beam

Let us consider a simply supported straight L-section beam structure of length L, shown in Fig. 12. The structure has equal legs ($W = H = 0.0508$ m) of uniform thickness $h = 0.0032$ m. Three different beam lengths of 0.25 m, 1 m and 4 m are considered. The structure is subjected to a prescribed axial displacement δ_x at point B in the $-x$ direction and the boundary conditions imposed are: $u_x = u_y = u_z = \theta_x = 0$ at point A and $u_y = u_z = 0$ at point B.

It should be noted that points A and B in Fig. 12 are eccentric with respect to the centroid (bending center) of the beam section. This eccentricity can be considered as an initial imperfection of the beam structures and can induce instability (or buckling) when the beam structure is slender enough. The position of the centroid in the $y - z$ plane is $y = z = 0.0127$ m in Fig. 12 and points A and B are at $y = z = 0.015$ m. Therefore, the eccentricity is $e_y = e_z = 0.0023$ m in the y and z directions.

We use a bilinear elastoplastic material model,

- Young's modulus: $E = 2 \times 10^{11}$ N/m^2,
- Yield stress: $\sigma_y = 250 \times 10^6$ N/m^2,
- Poisson's ratio: $v = 0.3$,
- Strain hardening modulus: $E_t = 0.1$ N/m^2.

Using the MITC9 shell finite elements, the three problems (corresponding to $L = 0.25$ m, 1 m and 4 m) described above are analyzed. Fig. 13 displays the non-scaled deformed shapes and accumulated effective plastic strain distributions of the simply supported L-section beam structures modeled using the MITC9 shell finite elements. In Fig. 13(b) and (c), plastic hinges are observed at mid length of the beam structures.

In the analysis using the L-section beam finite element, the 7-point per leg numerical integration is adopted as recommended in Section 3.1.2 and we use the 4, 8 and 16 uniform element meshes in the longitudinal direction.

Fig. 14(a) shows the reaction–displacement curves at the tip (point B in Fig. 12), when the beam length is 0.25 m. The axial reaction is measured at the same point where the displacement is prescribed. The curves represent typical linear elastic behavior up to point D in Fig. 14(a). After that point, yielding of the longitudinal fibers of the beam under compression occurs, which clearly governs the failure of this short beam. The results of the 2-node L-section beam finite element developed show almost the same curves as the solutions calculated from the shell finite element models.

The reaction–displacement curves of the 1.0 m beam are shown in Fig. 14(b). The behavior of this beam is more complex than the 0.25 m beam. Up to point D in the curves, the behavior is linear elastic. The beam then starts yielding and excessive bending develops at mid length of the beam where a plastic hinge suddenly occurs at point D. The plastic hinge and the $P - \Delta$ effect rapidly reduce the load-bearing capacity of the beam structure. The failure mode is dominated by plastic hinging and then the $P - \Delta$ effect.

The decreasing load-bearing capacity of this case can be explained by a simple model. When a simply supported beam with a plastic hinge buckles under a compressive load P, the plastic post-buckling response is approximately given by

$$P = \frac{2M_p}{\sqrt{L^2 - (L - \delta)^2}}, \tag{24}$$

where M_p is the plastic moment of the beam section, L is the length of the beam and δ is the axial displacement. This equation can be easily derived from the model in Fig. 15. We also plot the curve given by Eq. (24) in Fig. 14(b).

It is interesting to note that, in our numerical solution, there is a sudden change in the response curves of the shell finite element model (4×20 mesh) at point E but not in the beam finite element solutions. This behavior results from the local failure at the center of the beam structure due to the excessive deformation. Fig. 16 shows the deformed shape and accumulated effective plastic strain distributions before and after point E. A similar phenomenon happens in the numerical solution of the 2×20 mesh shell model but the position of the dropping point is different.

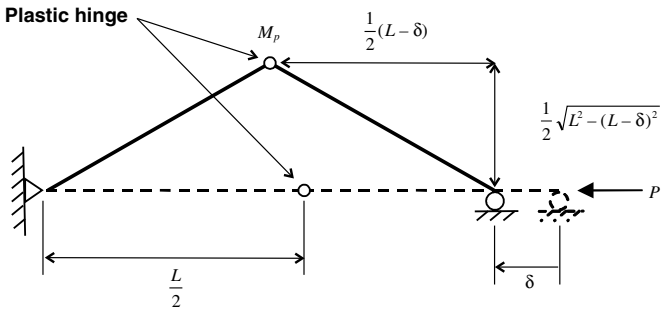

Fig. 15. Buckling of a simply supported beam with a plastic hinge at mid length.

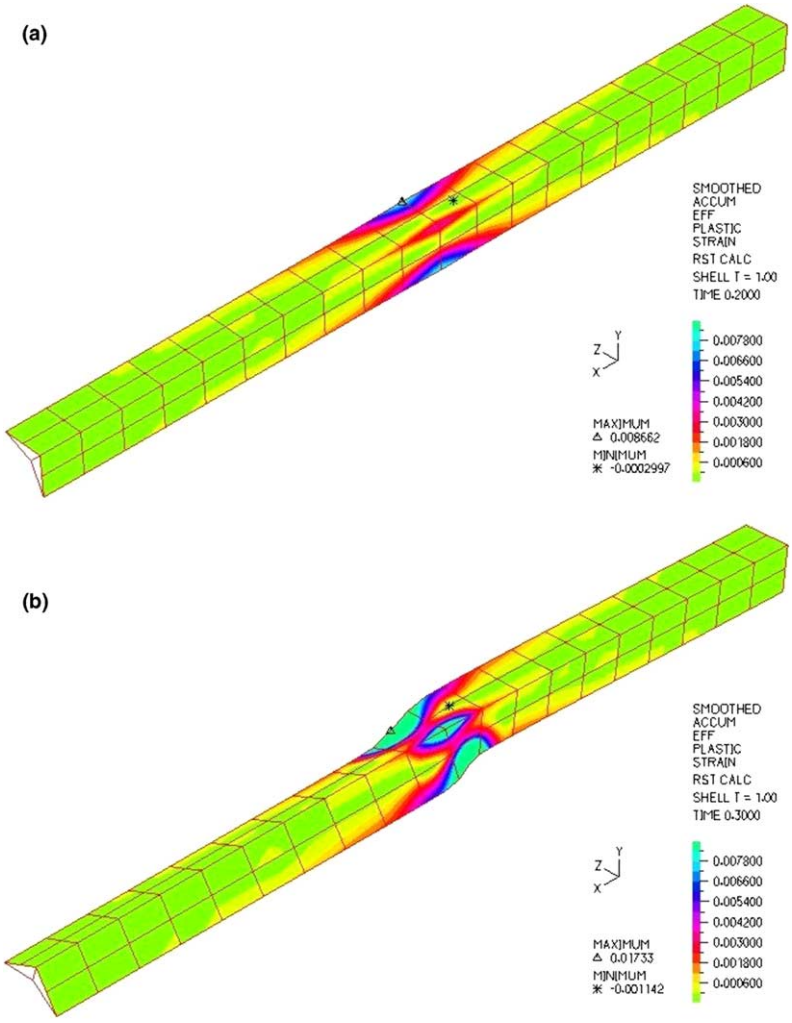

Fig. 16. Local failure at the mid length (a) before point E (b) after point E shown in Fig. 14(b).

The theoretical elastic buckling load of this beam is

$$P_{\mathrm{cr}} = \frac{\pi^2 E I_{\min}}{L^2} \approx 69,000\,\mathrm{N}, \tag{25}$$

where $I_{\min}$ is the minimum second moment of area of the beam section. However, the beam starts its failure when the reaction is about 60% of the buckling load because of the plastic hinge effect.

All the curves in Fig. 14(b) obtained from the beam and shell finite element models show a very similar response in the elastic range. However, after the plastic hinge occurs at the center of the beam structure, the beam finite element solutions show some difference with the results of the shell finite element models because of the local failure observed at mid length in the numerical solution of the shell models.

Fig. 14(c) shows the numerical results when the length of the beam structure is 4 m. Buckling of the beam structure starts at point D and the plastic hinge occurs at point E. The failure of this slender beam structure is clearly due to elastic buckling. The theoretical elastic buckling load calculated is $P_{\mathrm{cr}} \approx 4300$ N, which matches well with point D in the response curves. For the same reason as explained in the case of the 1.0 m beam structure, the solutions of the L-section beam finite element show different responses after dropping point F obtained with the shell finite element solution. It is also noted that Eq. (24) shows good agreement with the beam numerical solutions.

We report that, considering computational time required for comparable accuracy, the beam finite element model is about 2.5 times[2] efficient than the shell finite element model when the beam length is equal to 4 m. However, as the beam length decreases, the computational advantage of the beam finite element model becomes smaller.

As a last numerical example, we modeled the three simple beam problems with a section of unequal legs as shown in Fig. 17. The same prescribed axial displacements as in the previous example are applied at the shear center of the beam sections, that is, there is eccentricity. The same material properties are used and the 7-point per leg

[2] This ratio is obtained using the same solver in our analysis code for the beam and shell finite element models. Note that, in general, the ratio depends on a solver used to calculate the numerical solution.

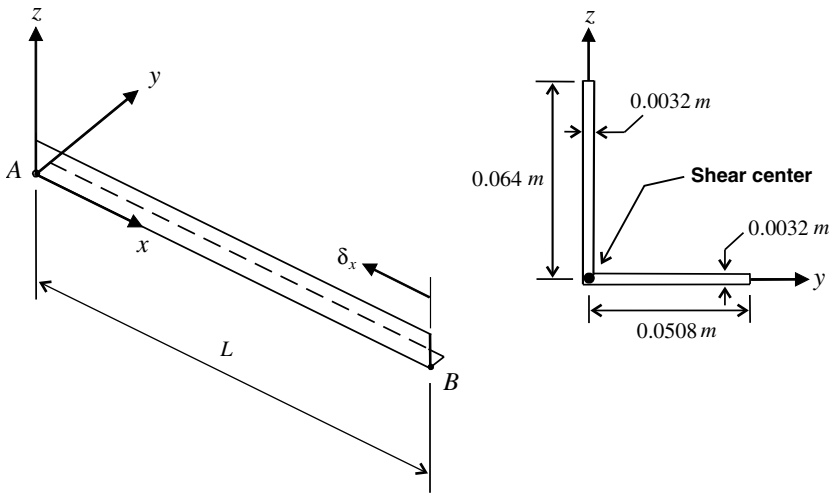

Fig. 17. A simply supported L-section beam with a section of unequal legs.

numerical integration is used for the beam finite element models. Fig. 18 shows the reaction–displacement curves in each case and the non-scaled deformed shape when the beam length L is equal to 1 m. It is observed that the reaction–displacement curves of the beam and shell finite element models show good agreement when eight beam finite elements are used.

Finally, we discuss when it is better to use the beam or shell finite element models. Considering the modeling effort and the computational time required to obtain an accurate solution, we find that for a simple structure with few L-section beam members, the beam finite element model is not much better than the shell finite element model. However, for structures with a large number of the L-section beam

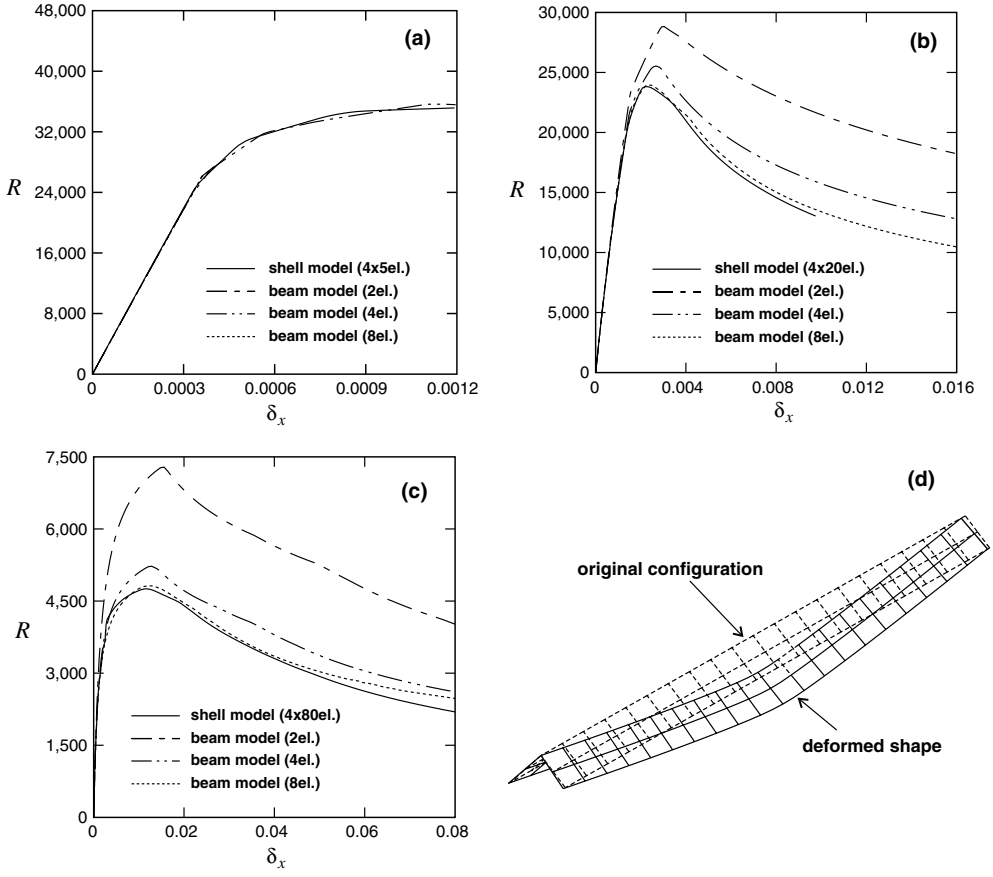

Fig. 18. Reaction–displacement curves for (a) $L = 0.25$ m, (b) $L = 1.0$ m and (c) $L = 4.0$ m, and (d) non-scaled deformed shape for $L = 1.0$ m and $\delta_x = 0.01$ m. (Unit for reaction is N and unit for displacement is m.)

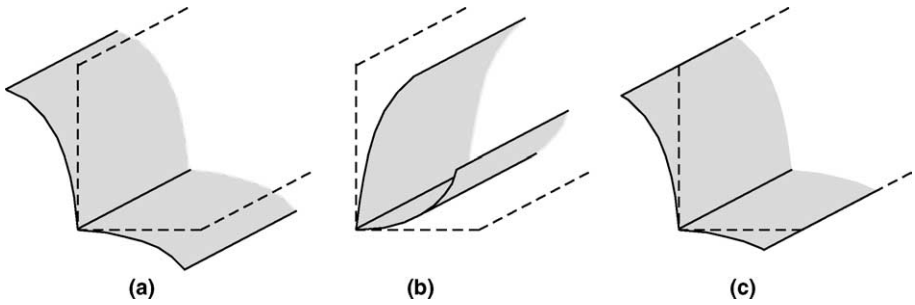

Fig. 19. Deformed shapes of the L-section beam structure which cannot be predicted by the beam finite element model.

members and for predicting the global responses, the beam finite element model is obviously much more efficient.

In inelastic large deformation analysis, it is important to note that the beam finite element model has its own limitations, mainly related to the basic kinematic assumption, that is, the plane cross-sections originally normal to the reference axis remain plane and undistorted during deformation. However, this assumption is violated in severe load cases and Fig. 19 shows the examples for L-section shapes. Therefore, the shell finite element model can better represent the realistic behavior of L-section beam structures, in particular, when the excessive local deformation needs to be investigated or the structure is simple to model.

4. Conclusions

The development of a general three-dimensional L-section beam finite element for elastoplastic large deformation analysis was presented and, for a numerical evaluation of the procedure proposed, the 2-node L-section beam finite element was implemented in an analysis code. Using this 2-node L-section beam finite element, we performed the elastic small and large deformation, and elastoplastic large deformation analyses of a cantilever structure subjected to various tip loadings. We then analyzed the failure of simply supported beam structures under elastoplastic large deformation.

The results were compared with the solutions obtained using a refined mesh of the MITC9 shell finite elements. In the numerical studies, we investigated the influence of the number of the beam finite elements used and the number of integration points (in elastoplastic analysis) on the solution accuracy. It was observed that the beam finite element solutions quickly converge to the reference solutions obtained with the refined shell finite element models, which demonstrates that the formulation of the 3D L-section beam finite element proposed is good and reliable. The numerical examples presented can be used as benchmark problems for other L-section beam finite elements developed in future.

The L-section beam finite element is very attractive in elastoplastic large deformation analysis because it requires much less modeling and computational effort than the shell finite element models for comparable accuracy, specially when structures with a large number of thin-walled beam members need to be analyzed. The formulation that we presented is general and effective as well as simple. The same procedure can be used to develop beam finite elements of other thin-walled sections regardless of their section shape and number of nodes. In this paper, the warping effect was ignored in the beam formulation but this subject would make a valuable study.

Acknowledgement

This work was funded by Hydro-Québec TransÉnergie. We are grateful that they have granted us permission to publish it.

References

[1] Bathe KJ. Finite element procedures. New York: Prentice Hall; 1996.
[2] Bathe KJ, Bolourchi S. Large displacement analysis of three-dimensional beam structures. Int J Numer Methods Eng 1979; 14:961–86.
[3] Chan SL, Kitipornchai S. Geometric nonlinear analysis of asymmetric thin-walled beam-columns. Eng Struct 1987;9:243–54.
[4] Turkalj G, Brnic J, Prpic-Orsic J. Large rotation analysis of elastic thin-walled beam type structures using ESA approach. Comput Struct 2003;81:1851–64.
[5] Bathe KJ. A simple and effective pipe elbow element—some nonlinear capabilities. Comput Struct 1983;17:659–67.
[6] Meek JL, Loganathan S. Geometric and material non-linear behaviour of beam-columns. Comput Struct 1990;34:87–100.
[7] Pi YL, Trahair NS. Nonlinear inelastic analysis of steel beam-columns. II: Applications. J Struct Eng 1994;120:2062–85.
[8] Lee PS, Bathe KJ. Development of MITC isotropic triangular shell finite elements. Comput Struct 2004;82:945–62.
[9] Argyris J. An excursion into large rotations. Comput Methods Appl Mech Eng 1982;32:85–155.
[10] ADINA R&D Inc. ADINA theory and modeling guide, 2003.
[11] Bathe KJ, Iosilevich A, Chapelle D. An evaluation of the MITC shell elements. Comput Struct 2000;75:1–30.
[12] Bathe KJ, Lee PS, Hiller JF. Towards improving the MITC9 shell element. Comput Struct 2003;81:477–89.